



**Ga<sub>4</sub>C-family crystals, a new generation of star thermoelectric materials, induced by band degeneracies, valley anisotropy, strong phonon scattering and others**

Journal:	<i>Journal of Materials Chemistry A</i>
Manuscript ID	TA-ART-11-2022-009210.R1
Article Type:	Paper
Date Submitted by the Author:	19-Feb-2023
Complete List of Authors:	Lou, Ao; School of Physics and Wuhan National High Magnetic Field Center, Huazhong University of Science and Technology Fu, Huahua; Huazhong University of Science and Technology, School of Physics Wu, Ruqian; University of California Irvine,

Cite this: DOI: 00.0000/xxxxxxxxxx

# Ga<sub>4</sub>C-family crystals, a new generation of star thermoelectric materials, induced by band degeneracies, valley anisotropy, strong phonon scattering and others

Ao Lou,<sup>a</sup> Hua-Hua Fu,<sup>\*,a</sup> and Ru-qian Wu<sup>b</sup>

Received Date

Accepted Date

DOI: 00.0000/xxxxxxxxxx

Using density functional theory combined with Boltzmann transport equation, we uncover a new class of high-performing thermoelectric material, i.e., supertetrahedral Ga<sub>4</sub>C-family materials characterized by ultrahigh thermoelectric figure of merit (*ZT*), which is produced both by large power factor and ultralow lattice thermal conductivity. The former is contributed by multiple electronic band degeneracies, flat bands and valley anisotropy; while the latter both by strong phonon scattering and low phonon group velocity. Furthermore, we find that tensile strain engineering may further suppress lattice thermal conductivity, while retains the multi-band degeneracies, valley anisotropy and flat bands well. In addition to the band degeneracy, the scattering mechanism of the system can also dominate the power factor in the process of strain implementation. Consequently, a novel thermoelectric phenomenon, i.e., high thermoelectric figure of merit, appears in Ga<sub>4</sub>C with a *ZT* value larger than 4.4 under a small strain ratio (0.75%). Our theoretical studies not only uncover a new class of high-performance thermoelectric materials integrated by multiple effective mechanisms, but also establish a realistic material plateau to investigate the competitive effect of multiple factors on enhancing thermoelectric figure of merit.

## 1 Introduction

Thermoelectric technology can directly and reversibly convert temperature gradient to electric voltage in solid-state materials<sup>1–5</sup>, and provides an effective way to harvest energy from waste heat or in special environments such as space<sup>6–10</sup>. However, low efficiency and high cost of current thermoelectric materials are still two crucial factors that hinder the exploitation of this technology<sup>11,12</sup>. The search or design new thermoelectric materials with high conversion efficiency is a urgent challenge in this field and has attracted increasing interdisciplinary search attention<sup>13,14</sup>. It is known that thermoelectric conversion efficiency is characterized by the so-called thermoelectric figure of merit

$ZT = S^2\sigma T / (k_l + k_e)$ , where *S* is Seebeck coefficient,  $\sigma$  is electrical conductivity, *T* is ambient temperature, *k<sub>l</sub>* and *k<sub>e</sub>* are lattice and electron thermal conductivity, respectively. As *S*,  $\sigma$ , and *k<sub>e</sub>* are mutually associated with each other, it is difficult to reach large *ZT* by regulating only one of these thermoelectric parameters and new strategies are required for the design of sustainable thermoelectric materials. Among two existing strategies, one is to improve their electronic properties by using band engineering, such as enhancing energy band convergence<sup>15,16</sup> or producing multiple valleys through band inversion<sup>17</sup>. The other is to reduce the lattice thermal conductivity, such as by introducing defect structures<sup>18,19</sup> or all-scale hierarchical architectures<sup>20–22</sup>. Unfortunately, it is still difficult to benefit from both of them in a single material, because high criteria on electronic and phononic transports are simultaneously required. To achieve unusually high thermoelectric performance, it is desired to construct new thermoelectric materials with different physical mechanisms.

<sup>a</sup> School of Physics and Wuhan National High Magnetic Field Center, Huazhong University of Science and Technology, Wuhan 430074, People's Republic of China.

<sup>b</sup> Department of Physics and Astronomy, University of California, Irvine, California 92697-4575, United States.

\* E-mail: hhfu@hust.edu.cn

Carbon is one of the earliest light elements ingrained and used by human beings, and has abundant allotropic phases with exceedingly rich physical features<sup>23,24</sup>. In particular, as the tetrahedral carbon atom in a diamond crystal is replaced by a C<sub>4</sub> tetrahedron, a new allotropic phase of carbon crystal, i.e., supertetrahedral carbon (T-carbon), can be constructed. T-Carbon has many unique physical properties<sup>25–27</sup> and additional advantages such as lower equilibrium density (1.5 g/cm<sup>3</sup>) and bulk modulus (169 GPa), which are suitable for device applications. Furthermore, its electronic and phononic properties can be tuned in a large range by substituting carbon with other elements such as boron (B), aluminium (Al), silicon (Si) and gallium (Ga). One may even replace entire C<sub>4</sub> tetrahedron to form supertetrahedral X<sub>4</sub>Y-family materials (where X is B, Al or Ga tetrahedron, Y is C or Si), which may have high band degeneracy and good transport properties<sup>28,29</sup>. This may overcome the drawbacks of T-carbon, e.g., the unwanted wide energy gap (~5 eV), and open a vista for the development of T-carbon as a new class of thermoelectric materials. With different substituents, X<sub>4</sub>Y can be engineered to have semiconductor or metal features and, meanwhile, the key advantages of T-Carbon such as low density and high hardness maintain well<sup>30–32</sup>. In particular, X<sub>4</sub>Y combinations may show much softer phonon dispersions due to the large mass mismatch and weaker covalent bond between X tetrahedra<sup>33,34</sup>. These unique properties and tunability support that X<sub>4</sub>Y-family materials may provide a chance to achieve ultrahigh thermoelectric figure of merit induced by multiple effective physical mechanisms.

In this work, we systematically study the electronic, phononic and transport properties of supertetrahedral Ga<sub>4</sub>C and directly calculate its thermoelectric coefficients. We uncover that the *p*-type Ga<sub>4</sub>C simultaneously possesses high electric conductance and large power factor  $S^2\sigma$ , owing to the large valley anisotropy and multiple-valley degeneracies with the high valley numbers  $N_V = 6$  at the point X and  $N_V = 12$  at the point W. Moreover, flat bands connecting these two valleys produce strong intervalley polar-optical-phonon scattering and thus impede electrons' mobility, significantly increasing the effective mass of electrons and the Seebeck coefficient. As a result, leading to a large power factor up to 6 mW m<sup>-1</sup>K<sup>-2</sup> at 300 K can be achieved. Meanwhile, due to low group velocity (less than 2.7 km/s) and low phonon lifetime (or high scattering rates), Ga<sub>4</sub>C exhibits ultralow lattice thermal conductivity,  $\kappa_l$  of 0.87 Wm<sup>-1</sup>K<sup>-1</sup> at room temperature. Benefiting both from high power factor and ultralow lattice thermal conductivity, the optimized value of  $ZT$  of Ga<sub>4</sub>C may reach up to 3.28 at 600 K, larger than almost all  $ZT$  values reported to date under the same conditions<sup>35</sup>.

Another inspiring finding is that tensile strain engineering may further enhance the phonon scattering and reduce  $\kappa_l$  in Ga<sub>4</sub>C,

**Table 1** Three types of electron scattering mechanism are considered as implemented in AMSET: (i) acoustic deformation potential (ADP); (ii) ionized impurity (IMP); (iii) polar-optical phonon (POP).  $\tau_T$  are the lifetimes for a given scattering process at  $T$  in unit of fs where hole concentration is assumed to be  $4 \times 10^{19}$  cm<sup>-3</sup>,  $\alpha_V^{\text{VBM}}$  and  $\alpha_V^{\text{CBM}}$  are the volume deformation potential of valence band maximum (VBM) and conduction band minimum (CBM) in unit of eV,  $B_0$  is the bulk modulus in unit of GPa,  $Z$  is the charge of electron donor dopant,  $\epsilon_0$  is the static dielectric constant,  $\epsilon_\infty$  is the electronic contribution to the static dielectric constant, and  $\omega_{po}$  is the polar-optical phonon frequency in THz.

ADP	$\tau_{300}$ 150.6	$\tau_{500}$ 90.9	$\alpha_V^{\text{VBM}}$ -0.05	$\alpha_V^{\text{CBM}}$ -1.29	$B_0$ 40.04
IMP	$\tau_{300}$ 107.4	$\tau_{500}$ 73.5	$Z$ 1	$\epsilon_0$ 11.61	
POP	$\tau_{300}$ 31.7	$\tau_{500}$ 21.1	$\omega_{PO}$ 12.01	$\epsilon_\infty$ 8.68	$\epsilon_0$ 11.61

while retain the multi-valley degeneracies and unique flat bands. Theoretical calculations show that  $\kappa_l$  of Ga<sub>4</sub>C decreases to an ultralow value 0.577 (0.398) Wm<sup>-1</sup>K<sup>-1</sup>, even a small tensile strain is applied, such as 0.5% (0.75%). Although tensile strain does not alter band degeneracies near the Fermi level, the power factor is still decreased as a whole, because it enhances the polar-optical-phonon scattering and hence, reduces the the lifetimes of electron's transport and the electric conductivity. As a result, a higher thermoelectric figure of merit, with a  $ZT$  value larger than 4.5 at 600 K, occurs in Ga<sub>4</sub>C under a 0.75% tensile strain. This work reveals several new physical mechanisms to enhance the thermoelectric figure of merit and provides an excellent class of high-performing thermoelectric materials for practical uses.

## 2 First-principle calculations and Boltzmann transport equations

The crystal structures of supertetrahedral Ga<sub>4</sub>C, as an example of X<sub>4</sub>Y-family materials, are fully optimized by utilizing the density functional theory (DFT) based on the projector augmented wave method, as implemented in Vienna *ab initio* Simulation Package (VASP)<sup>36</sup>. To perform all DFT calculations, the generalized gradient approximation (GGA) in the form of Perdew-Burke-Ernzerhof (PBE) functional is chosen as the exchange correlation potential<sup>37</sup>. The energy cutoff for the plane-wave expansion is set to be 700 eV and a Monkhorst-Pack k-mesh of  $11 \times 11 \times 11$  is used in the first Brillouin zone (BZ). Each ionic iteration step converges at an energy criterion of  $10^{-8}$  and an accurate optimization of structural parameters is employed by minimizing the interionic forces less than  $10^{-3}$  eV/Å. The electronic band structures of material samples are calculated by hybrid DFT within the framework of Heyd-Scuseria-Ernzerhof (HSE) based on the relaxed structures.

Furthermore, the phononic band structures, the dynamic stability analysis and harmonic IFCs of the sample Ga<sub>4</sub>C are performed by using the Phonopy code with a finite-displacement step of 0.01 Å<sup>3</sup>. There are three symmetries reduced displacements considered for the 2 × 2 × 2 supercell containing 40 atoms and the Brillouin sampling is set to be 7 × 7 × 7. Moreover, we choose a 3 × 3 × 3 supercell and a cutoff radius of 0.7 nm to obtain anharmonic IFCs, the *q*-points mesh is employed as 21 × 21 × 21 to obtain a converged lattice thermal conductivity as implemented in ShengBTE package<sup>38</sup>.

The electronic transport properties of all supertetrahedral Ga<sub>4</sub>C samples are calculated by solving linearized Boltzmann transport equation (BTE) with the nonempirical carrier lifetime derived from Fermi's golden rule<sup>39</sup>. The linearized BTE gives the definition of electrical transport distribution function as below

$$\sum_{\alpha\beta}(\varepsilon) = \sum_{ik} \tau_{ik} v_{\alpha}(ik) v_{\beta}(ik) \frac{\delta(\varepsilon - \varepsilon_{ik})}{d\varepsilon}, \quad (1)$$

where  $\varepsilon$  is the electronic energy,  $\alpha$  and  $\beta$  denote Cartesian coordinates,  $v$  is the energy group velocity of band index  $i$  and wave vector  $k$ . The Seebeck coefficient ( $S$ ) and the electrical conductivity ( $\sigma/\tau$ ) can be obtained by

$$\sigma_{\alpha\beta} = e^2 \int \sum_{\alpha\beta}(\varepsilon) \left[ -\frac{\partial f^0}{\partial \varepsilon} \right] d\varepsilon, \quad (2)$$

$$S_{\alpha\beta} = \frac{1}{eT} \frac{\int \sum_{\alpha\beta}(\varepsilon) (\varepsilon - \varepsilon_F) \left[ -\frac{\partial f^0}{\partial \varepsilon} \right] d\varepsilon}{\int \sum_{\alpha\beta}(\varepsilon) \left[ -\frac{\partial f^0}{\partial \varepsilon} \right] d\varepsilon}. \quad (3)$$

Within the Born approximation, the scattering rates  $\tau_{ik}^{-1}$  in Eq. (1), when the  $i$ th electron at the initial state  $ik$  couples with the phonon with the wave vector  $q$  and frequency  $\omega_q$  and transfers to the final state of  $jk + q$ , can be defined by Fermi's golden rule according to their elastic or inelastic nature as elastic scattering rates

$$\tau_{ik \rightarrow (jk+q)}^{-1} = \frac{2\pi}{\hbar} \langle jk+q | g_{ij} | ik \rangle^2 \delta(\varepsilon_{ik} - \varepsilon_{jk+q}), \quad (4)$$

and the inelastic scattering rates

$$\begin{aligned} \tau_{ik \rightarrow (jk+q)}^{-1} &= \frac{2\pi}{\hbar} \langle jk+q | g_{ij} | ik \rangle^2 \\ &\times \left[ (n_q + 1 - f_{jk+q}^0) \delta(\varepsilon_{ik} - \varepsilon_{jk+q} - \hbar\omega_q) \right. \\ &\left. + (n_q + f_{jk+q}^0) \delta(\varepsilon_{ik} - \varepsilon_{jk+q} + \hbar\omega_q) \right], \end{aligned} \quad (5)$$

where  $g_{ij}$  represents the electron-phonon coupling matrix due to the acoustic deformation potential (ADP), ionized impurity po-

tential (IMP), and polar-optical phonon (POP) scattering mechanisms are considered

$$g_{ij}^{\text{ADP}}(k, q) = \left[ \frac{k_B T \alpha_V^2}{B_0} \right]^{\frac{1}{2}} \langle \Psi_{jk+q} | \Psi_{ik} \rangle, \quad (6)$$

$$g_{ij}^{\text{IMP}}(k, q) = \left[ \frac{n Z^2 e^2}{\varepsilon} \right]^{\frac{1}{2}} \frac{\langle \Psi_{jk+q} | \Psi_{ik} \rangle}{|q|^2 + \beta^2}, \quad (7)$$

$$g_{ij}^{\text{POP}}(k, q) = \left[ \frac{\hbar \omega_{\text{PO}}}{2} \left( \frac{1}{\varepsilon_{\infty}} - \frac{1}{\varepsilon_0} \right) \right]^{\frac{1}{2}} \frac{\langle \Psi_{jk+q} | \Psi_{ik} \rangle}{|q|}. \quad (8)$$

Then, the total scattering time  $\tau_e$  is defined as

$$\frac{1}{\tau_e} = \frac{1}{\tau^{\text{ADP}}} + \frac{1}{\tau^{\text{IMP}}} + \frac{1}{\tau^{\text{POP}}}. \quad (9)$$

The formalism is implemented in the ab initio scattering and transport (AMSET) package<sup>40</sup>. The required material parameters for the crystal Ga<sub>4</sub>C, including dielectric constants  $\varepsilon$ , phonon frequency  $\omega$ , bulk modulus  $B_0$ , deformation potential  $\alpha$ , are obtained from the first-principles calculations as given in Table 1.

## 3 Results and discussion

### 3.1 Crystal structure and basic bulk properties

Figures 1(a) and 1(b) show the crystal structure in a cubic unit cell and the first Brillouin zone (BZ) of the supertetrahedral Ga<sub>4</sub>C, respectively. The crystal has a diamond-like structure and the carbon atom with the Wyckoff coordinates (0.25 0.25 0.25) being replaced by a Ga tetrahedron. The primitive cell has four Ga atoms and one C atom with the spatial group  $Fd\bar{3}m$ . The full structural optimization gives a lattice parameter of 8.211 Å for the cubic cell, and the Wyckoff coordinates of Ga atoms are 32e ( $x, x, x$ ) with  $x = 0.1396$  Å. The bond length between two nearest neighboring Ga atoms is 2.563 Å, and that between neighboring Ga and C atoms, 1.985 Å. To examine the existence of the crystal Ga<sub>4</sub>C, we calculated its formation energy  $E_{\text{form}}$  by the following relation:

$$E_{\text{form}} = E_{\text{Ga}_4\text{C}} - 4E_{\text{Ga}} - E_{\text{C}}, \quad (10)$$

where  $E_{\text{Ga}_4\text{C}}$  denotes the energy of Ga<sub>4</sub>C in a unit cell,  $E_{\text{Ga}}$  and  $E_{\text{C}}$  denote the chemical potential of Ga atom and C atom, respectively. Our calculation demonstrates that the formation energy of Ga<sub>4</sub>C is characterized by a negative value (i.e., -0.06371 eV/atom), indicating the existence of the supertetrahedral Ga<sub>4</sub>C studied here.

From the calculated electronic band structure in Fig. 1(c), one may see that Ga<sub>4</sub>C is a semiconductor characterized by a modest indirect band gap ( $E_g = 1.30$  eV). For comparison, the band

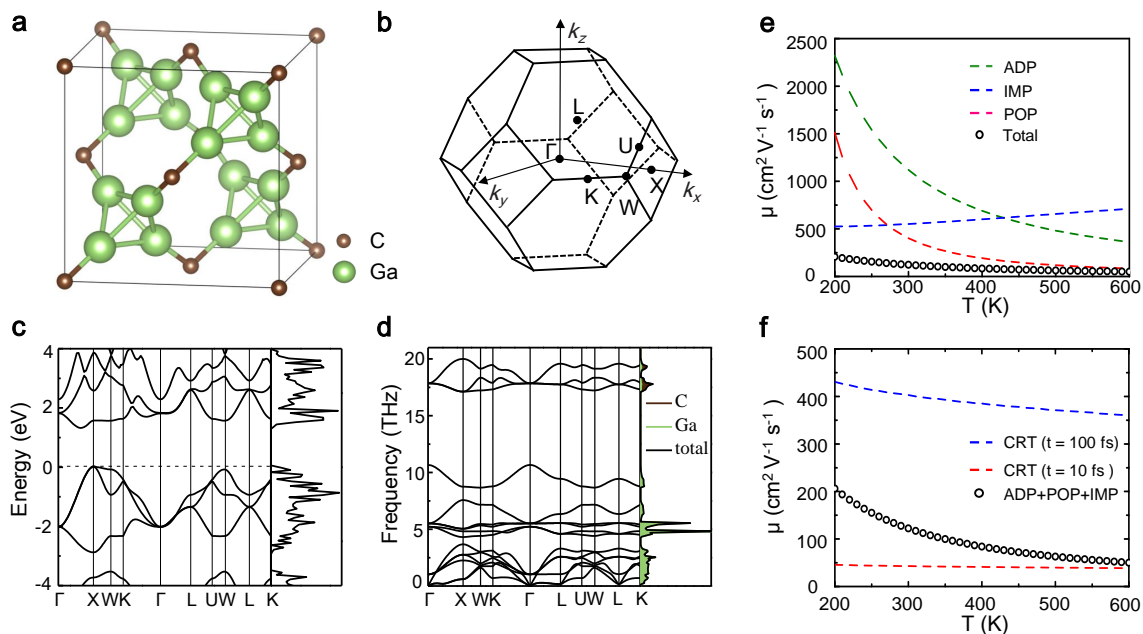


**Fig. 1** Crystal structure of  $\text{Ga}_4\text{C}$  and its electronic and phononic properties. (a) Crystal structure in a unit cell and (b) the corresponding first BZ. (c) Electronic band structure of  $\text{Ga}_4\text{C}$  along the high-symmetry paths together with the related electronic density of states (DOSs) in the first BZ. (d) Phononic band structure and the related phononic DOSs, where the contributions from C and Ga atoms are denoted by the brown and aqua lines, respectively. (e) Electronic mobility of  $\text{Ga}_4\text{C}$  at a electron concentration of  $3 \times 10^{18} \text{ cm}^{-3}$  as a function of temperature. The mobility limited by acoustic deformation potential (ADP), ionized impurity (IMP), and polar optical phonon (POP) scattering process are indicated by the orange, blue and red dashed lines. The black circle markers show the mobility where all three scattering processes are considered. (f) Comparison between the constant relaxation time (CRT) approximation and the ab-initio scattering approach. Blue and red dash lines denote the mobility calculated based on the CRT approximation where relaxation time is set as 10 and 100 fs, respectively. The black circles denote the mobility obtained from the ab-initio calculations (ADP+IMP+POP).

structure calculated from the PBE functional (see Sec. A in Supplementary Information (SI)) shows a band gap of 0.80 eV. Its conduction band minimum (CBM) is between  $\Gamma$  and X, and the valence band maximum (VBM) is at X. Interestingly, another valence band is very close to the VBM at W with a small offset energy of 0.105 eV, which should also contribute to electronic conductivity in hole doping. Moreover, there is a flat band along the path X-W, connecting two neighboring valleys. This is much different from the ring-shaped and Mexican-hat-shaped bands regarded as the curial factors responsible for large power factors in some materials<sup>41–44</sup>. Importantly, the VBM at X show a high valley degeneracy with valley number  $N_v = 6$  and the one at W has  $N_v = 12$ . The multi-valley degeneracy is a distinctive feature of  $\text{Ga}_4\text{C}$ , and is expected to lead to large  $\sigma$ . Additionally, the special four-corners-star Fermi surface contributed by flat bands (see Fig. S1(b) in Sec. A, SI) provides another advantage for developing  $\text{Ga}_4\text{C}$  as a potential high-performance thermoelectric material.

The phononic bands of  $\text{Ga}_4\text{C}$  are shown Fig. 1(d). We find that no branch has negative phonon frequency and this property

maintains in all phonon branches along other directions, indicating that  $\text{Ga}_4\text{C}$  is dynamically stable in the diamond-like structure. The phononic density of states (DOSs) further demonstrate that phononic bands in the low-frequency region are contributed mainly by Ga atoms, while bands in the high-frequency region mainly by C atoms. Moreover, most phononic bands are much flat, especially the acoustic branches as well as low-frequency optical modes between 1.0 and 7.0 THz, indicating their low group velocities. In particular, a dense block of low-energy phonon branches can be found in the frequency range of 1.0–3.7 THz, and these acoustic branches couple with each other and create rich momentum scattering pathways. These features are expected to reduce the lifetime of heat-carrying acoustic modes and drastically decrease lattice thermal conductivity for the benefit of high thermoelectric performance. Additionally, we well know that the avoided crossing between optical and acoustic branches is essential for phonon scattering, which is an important factor to influence the thermal conductance of any thermoelectric material. Through carefully checking all phonon bands, we find that the

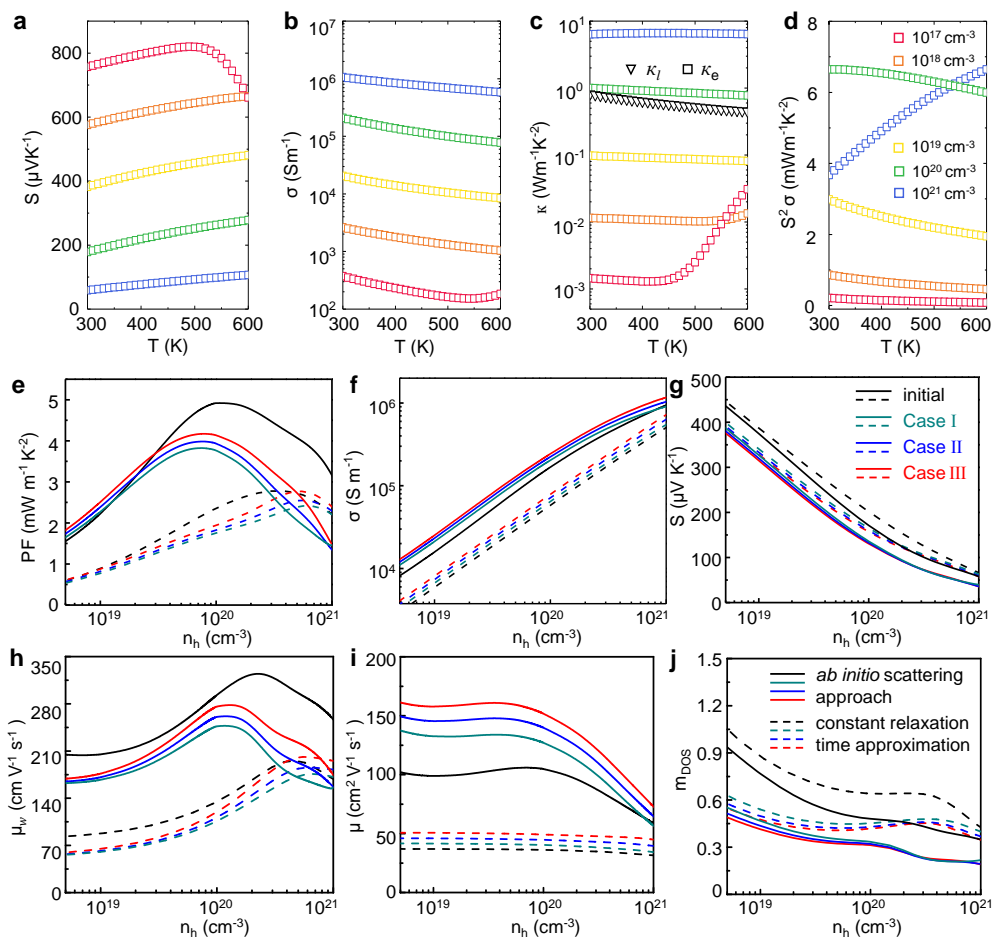


**Fig. 2** Electronic transport properties and the related thermoelectric parameters in  $\text{Ga}_4\text{C}$ . (a)-(d) The Seebeck coefficient  $S$ , electronic conductance  $\sigma$ , electronic thermal conductance  $\kappa_e$  and power factor  $S^2\sigma$  in  $\text{Ga}_4\text{C}$  versus the temperature  $T$  are shown respectively. (e)-(g) Power factor  $\text{PF}$  ( $S^2\sigma$ ),  $\sigma$  and  $S$  versus the hole concentration  $n_h$  in the  $p$ -type band configurations at  $T=300$  K. (h)-(j) Weighted mobility  $\mu_w$ , electrons' mobility  $\mu$  and the effective mass density of states  $m_{\text{DOS}}$  versus  $n_h$  in the same band configurations and under the same temperature are shown, respectively.

avoided crossing between optical and acoustic branches also displays in phonon dispersions, indicating the reliability of our calculations on phonon scattering and the related thermal conductance in  $\text{Ga}_4\text{C}$ .

### 3.2 Ultrahigh power factor and large Seebeck coefficient

To understand the key characteristics of electronic transport in  $\text{Ga}_4\text{C}$ , we discuss three scattering mechanisms, i.e., acoustic deformation potential (ADP), ionized impurity (IMP) and polar-optical phonon (POP). The electron relaxation times and other properties are given in Table 1. In Fig. 1(e), the electronic mobility  $\mu$  under the influence of these three scattering mechanisms and with the total scattering time  $\tau_e$  (defined in Eq. (9)) are pre-

sented. The numerical results demonstrate that the electron mobility of  $\text{Ga}_4\text{C}$  is dominated by POP, while little by ADP scattering, originating from the small valence-band-edge deformation potential in this material. Moreover, the comparison with results from the constant-relaxation-time (CRT) approximation are provided in Fig. 1(f), where the relaxation time is set as  $\tau=10$  and  $100$  fs, confirming further the above conclusion. This particular feature of electronic mobility has also been found in some polar semiconductors, including two star thermoelectric materials:  $\text{PbTe}$ <sup>45</sup> and  $\text{SnSe}$ <sup>46</sup>, and is regarded as one of key factors responsible for their ultrahigh thermoelectric figure of merit.

The Seebeck coefficient  $S$ , electrical conductivity  $\sigma$ , thermal conductivity  $\kappa$  and power factor  $S^2\sigma$  versus temperature under different hole concentrations ( $n_h$ ) are provided in Figs. 2(a)-2(d),

where  $n_h$  varies from  $10^{17}$  to  $10^{21}$   $\text{cm}^{-3}$ . The corresponding thermoelectric coefficients versus electron doping  $n_e$  are also drawn in Figs. S2(a)-(d) in Sec. B, SI. We find that  $S$  in both  $p$ - and  $n$ -doping  $\text{Ga}_4\text{C}$  decreases as  $n_h$  or  $n_e$  increases, while  $S$  in the former is larger than that in the latter, due to the larger effective mass in valence bands near the Fermi level. Moreover,  $\sigma$  in the  $p$ -type  $\text{Ga}_4\text{C}$  ranges from  $\sim 265$  to  $\sim 9.14 \times 10^5$   $\text{Sm}^{-1}$  at room temperature, much larger than the corresponding values in the  $n$ -type doping, which may be due to the anisotropic parabolic band edge<sup>47</sup>. Therefore, the large Seebeck coefficient and high conductivity result in high power factor reaching up to 6  $\text{mW}/(\text{mK}^2)$  in the  $p$ -type  $\text{Ga}_4\text{C}$  with  $n_h = 10^{20}$   $\text{cm}^{-3}$ .

It is reported that the bands with heavy-effective mass near the Fermi level can lead to a large Seebeck coefficient, and while the bands with light-effective mass may contribute to a high electric conductivity. Obviously, there exists a controversy about the role of bands with different effective masses on thermoelectric performance of materials. Here, thanks to the correlation between the electronic mobility and the different kinds of effective masses in  $\text{Ga}_4\text{C}$ , we may make clear this issue. Note that when the multi-valleys' electronic conduction is considered, the electronic mobility in non-degenerate bands can be expressed as

$$\mu = \frac{2^{3/2} \pi^{1/2} \hbar^4 e C_1}{3 m_{\parallel} (m_b k_B T)^{3/2} \Xi^2}, \quad (11)$$

where  $m_b = (m_{\parallel} m_{\perp})^{1/3}$  is the effective band mass and  $m_{\parallel} = \frac{3m_{\parallel} m_{\perp}}{2m_{\perp} + m_{\parallel}}$  is the inertial effective band mass with  $m_{\parallel}$  and  $m_{\perp}$  named radial mass and longitudinal mass, respectively. Obviously, larger  $m_b$  is beneficial to enhance  $S$  and smaller  $m_{\parallel}$  beneficial to increase  $\mu$ . Moreover, one may obtain their relation as below

$$m_b/m_{\parallel} = \frac{2m_{\perp} + m_{\parallel}}{3(m_{\parallel} m_{\perp}^2)^{1/3}} = \frac{2}{3} r^{1/3} + \frac{1}{3} r^{-2/3}, \quad (12)$$

where the large mass ratio  $r$  can significantly enhance the power factor. Due to the appearance of strong valley anisotropy in  $\text{Ga}_4\text{C}$ , the band mass  $m_b$  along  $\Gamma$ -X direction ( $m_b = 0.041 m_e$ ) is much smaller than that along X-W direction ( $m_b = 0.3165 m_e$ ). Therefore, by modifying band shape near the Fermi level along the high-symmetry path W-X (see Fig. S3 in Sec. C, SI), one may realize various conduction bands characterized by different band effective masses<sup>48</sup>. Here, we design three bands with different  $m_b$ : i.e., the first band with a large  $m_b$  (Case I:  $m_b = 0.0459 m_e$ ), the second band with a middle  $m_b$  (Case II:  $m_b = 0.0326 m_e$ ) and the third band with a small  $m_b$  (Case III:  $m_b = 0.0249 m_e$ ). Moreover, the initial flat band is also considered here for comparison.

We first analyze the weighted mobility  $\mu_W$ <sup>49</sup>, which is defined by electronic mobility  $\mu$  and effective mass density-of-state (DOS)

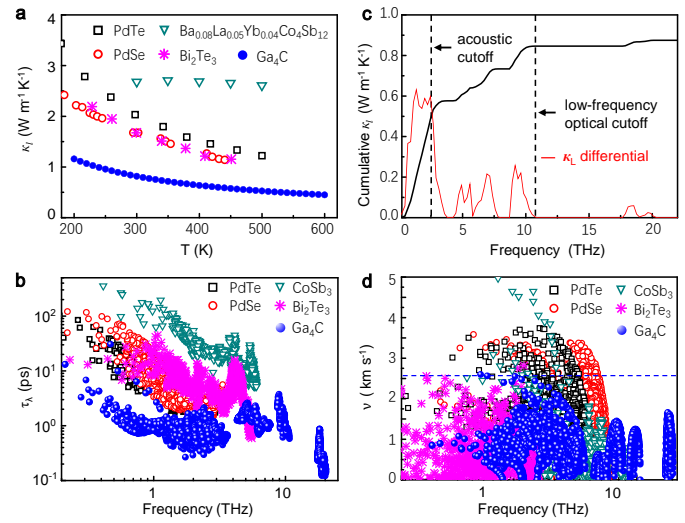


**Fig. 3** Phononic transport properties and the related thermoelectric parameters in  $\text{Ga}_4\text{C}$ . (a) Lattice thermal conductivity  $\kappa_l$  versus temperature. (b) Phonon lifetime  $\tau_\lambda$  versus the frequency at  $T=300$  K. For comparison, the associated values of  $\tau_\lambda$  in other four famous thermoelectric materials, i.e., PdTe, PdSe,  $\text{Ba}_{0.08}\text{La}_{0.05}\text{Yb}_{0.04}\text{Co}_4\text{Sb}_{12}$  and  $\text{Bi}_2\text{Te}_3$  are also provided. (c) Cumulative lattice thermal conductivity  $\kappa_l$  and its differential with respect to the phonon frequency. (d) Phonon group velocity  $v$  of  $\text{Ga}_4\text{C}$  and the above four thermoelectric materials versus the phonon frequency.

as  $\mu_{\text{DOS}} = \mu m_{\text{DOS}}^{2/3}$  (see Sec. D in SI). The typical thermoelectric coefficients PF,  $\sigma$  and  $S$  versus  $n_h$  for these four band configurations are drawn in Figs. 2(e)-(g), and the associated parameters  $\mu_W$ ,  $\mu$  and  $m_{\text{DOS}}$  in Figs. 2(h)-(j). The solid and dotted lines denote the *ab initio* scattering approach and the constant-relaxation-time (CRT) approximation, respectively, and different colors are used for different configurations. One may see that PF and  $\mu_W$  display similar changing behaviors in both approaches. To distinguish their behaviors further, we set the constant relaxation time to be 20 fs, and find that nearly all thermoelectric parameters obtained from *ab initio* scattering approach are larger than those from CRT approximation. More importantly, both approaches give the same conclusion that among the four band configurations, the original flat bands have the largest values of PF,  $S$ ,  $\mu_W$  and  $m_{\text{DOS}}$ , but small  $\sigma$  and  $\mu$ . To understand the underlying physics, we should further consider different inter-valley scattering mechanisms with the four band configurations, and details are given in Sec. C in SI. We find that aside from band degeneracies, the carrier's scattering in the flat bands between two neighboring valleys also works as an effective mechanism for getting large Seebeck coefficient and enhanced power factor in  $\text{Ga}_4\text{C}$ .

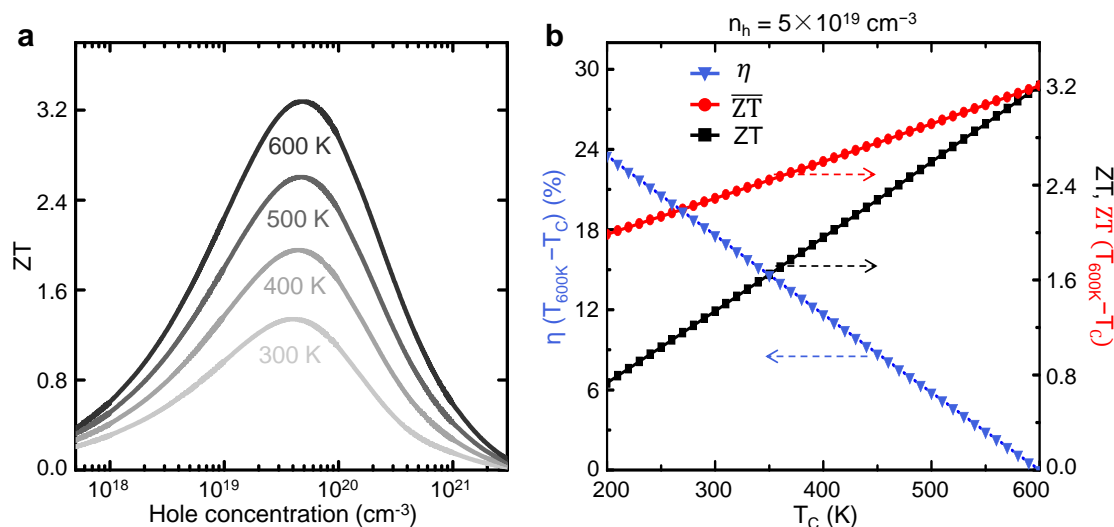


**Fig. 4** Thermoelectric figure of merit  $ZT$  and efficiency prediction in  $\text{Ga}_4\text{C}$ . (a) predicted  $ZT$  values of  $\text{Ga}_4\text{C}$  as a function of temperature and hole concentration. (b) Estimated thermoelectric efficiency  $\eta$ ,  $ZT$  and its average value  $\overline{ZT}$  at hole concentration  $n_h = 5 \times 10^{19} \text{ cm}^{-3}$  over the temperature range of  $T_h$ - $T_c$ , where  $T_h$  is fixed as 600 K.

### 3.3 Ultralow lattice thermal conductivity and the underlying physical mechanisms

Aside from the ultrahigh power factor and large Seebeck coefficient, it is important that ultralow  $\kappa_l$  also occurs in  $\text{Ga}_4\text{C}$ . As described in Fig. 1(d), some optical branches in  $\text{Ga}_4\text{C}$  have extremely low frequencies and many acoustic branches are nearly flat bands. These peculiar phononic features provide key conditions to generate ultralow  $\kappa_l$ . Quantitatively, our theoretical calculations demonstrate that  $\kappa_l$  of  $\text{Ga}_4\text{C}$  is exceptionally low, to merely  $0.87 \text{ Wm}^{-1}\text{K}^{-1}$  at 300 K and  $0.44 \text{ Wm}^{-1}\text{K}^{-1}$  at 600 K, as shown in Fig. 3(a). It should be stressed that some values of  $\kappa_l$  in the  $p$ -type  $\text{Ga}_4\text{C}$  are even smaller than the corresponding values of electron thermal conductivity  $\kappa_e$  (see Fig. 2(c)). To highlight the ultralow  $\kappa_l$  obtained here, in Fig. 3(a), we give the related values of  $\kappa_l$  of some other popular high-performance thermoelectric materials, such as  $\text{PdTe}$ <sup>50</sup>,  $\text{PdSe}$ <sup>51</sup>,  $\text{Ba}_{0.08}\text{La}_{0.05}\text{Yb}_{0.04}\text{Co}_4\text{Sb}_{12}$ <sup>52</sup>, and  $\text{Bi}_2\text{Te}_3$ <sup>53</sup> under the similar conditions. It is obvious that  $\kappa_l$  of  $\text{Ga}_4\text{C}$  is remarkably lower, even by an order of magnitude, than the values of  $\kappa_l$  of other thermoelectric materials.

To uncover the underlying physics for the ultralow  $\kappa_l$  in  $\text{Ga}_4\text{C}$ , we study the phonon transport via phenomenological modeling. It has been established that the acoustic phonon lifetime  $\tau_\lambda$  is the key parameter to determine the thermal conduction. A general rule is that the shorter  $\tau_\lambda$  is, the lower  $\kappa_l$  appears in materials. Figure 3(b) shows  $\tau_\lambda$  versus the phonon frequency in  $\text{Ga}_4\text{C}$ . For a comparable study,  $\tau_\lambda$  in other well-known thermoelectric mate-

rials, such as  $\text{PdTe}$ <sup>54</sup>,  $\text{PdSe}$ <sup>54</sup>,  $\text{Ba}_{0.08}\text{La}_{0.05}\text{Yb}_{0.04}\text{Co}_4\text{Sb}_{12}$ <sup>55</sup> and  $\text{Bi}_2\text{Te}_3$ <sup>56</sup>, are also provided. One can see that a unique thermal transport property occurs in  $\text{Ga}_4\text{C}$ , i.e.,  $\tau_\lambda$  in  $\text{Ga}_4\text{C}$  is remarkably shorter than those in other thermoelectric materials mentioned above, indicating that  $\text{Ga}_4\text{C}$  exhibits extremely short acoustic phonon lifetime, even lower than 1 ps in most frequency regions. Moreover, from the numerical results of cumulative  $\kappa_l$  versus the frequency (see Fig. 3(c)), we find the lattice thermal conductance is dominated by the acoustic bands in the low-frequency region, which confirms further that the strong phonon scattering in  $\text{Ga}_4\text{C}$  benefits to its low  $\kappa_l$ .

On the other side, we well know that phonon group velocity  $v$  is another important parameter to influence the lattice thermal conductance in thermoelectric materials. It is interesting that several nearly flat phonon bands appear in the acoustic branches of  $\text{Ga}_4\text{C}$ , indicating that the low-frequency phonon bands tend to possess low phonon group velocity. In Fig. 3(d), we drawn the numerical results of phonon group velocity as a function of frequency in  $\text{Ga}_4\text{C}$  and meanwhile, the phonon group velocity of above four thermoelectric materials are also provided for comparisons. One can see that the maximum phonon group velocity ( $\sim 2.52 \text{ km/s}$ ) in  $\text{Ga}_4\text{C}$  is much smaller than the related values in other four thermoelectric materials. Thus we believe that the low phonon group velocity in  $\text{Ga}_4\text{C}$  works as another effective mechanism for its ultralow lattice thermal conductance.

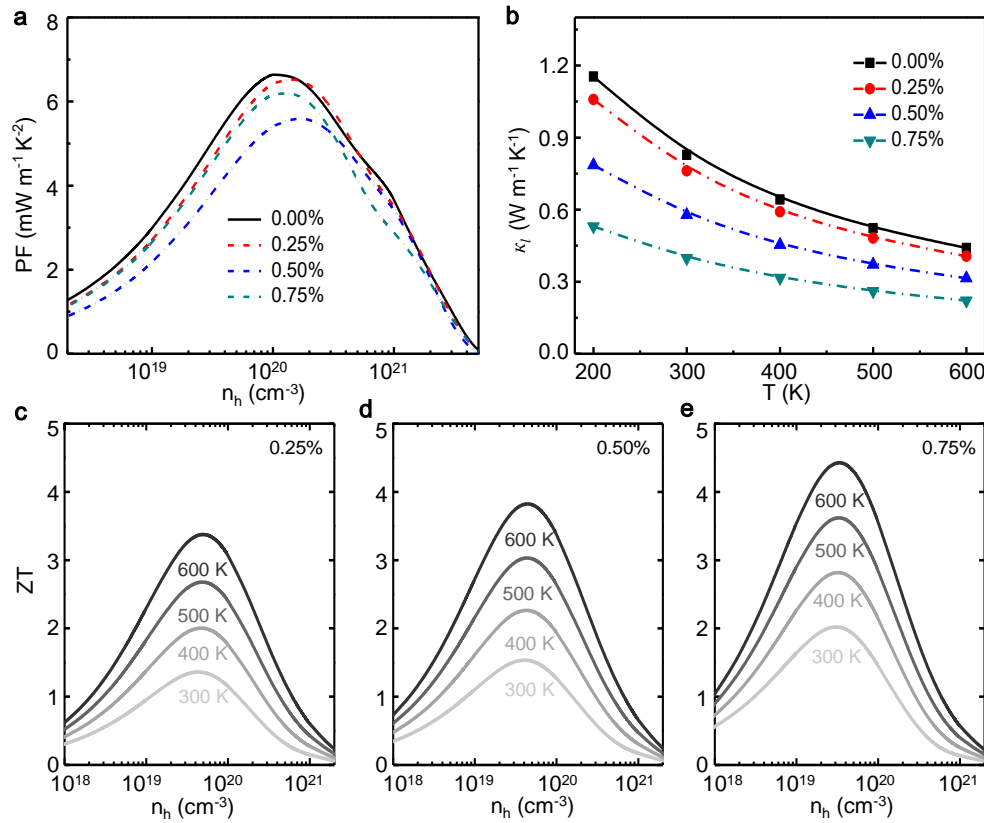


**Fig. 5** Large enhancement of ZT by the tensile strain engineering. (a) and (b) Power factor PF versus the hole concentration  $n_h$  and lattice thermal conductance  $\kappa_l$  versus temperature under the tensile strain ratio 0.0%, 0.5%, 0.75% and 1.0%. (c) and (e) The thermoelectric figure of merit ZT versus  $n_h$  and temperature under the tensile strain ratio 0.5%, 0.75% and 1.0%, respectively.

### 3.4 High thermoelectric conversion efficiency

In what follows, we turn to appreciate the high-performance thermoelectric figure of merit (ZT) in Ga<sub>4</sub>C, since both high power factor and low lattice thermal conductivity are obtained. Firstly, we should shed light on the safe working temperatures for the crystal Ga<sub>4</sub>C to work as a thermoelectric material with high ZT. A previous literature demonstrates that the melting temperature of Ga<sub>4</sub>C lies in the range from 600 to 700 K<sup>28</sup>. Moreover, by using molecular dynamic simulation, we also calculate the pair-correlation function (PCF) for the crystal Ga<sub>4</sub>C at temperature 650 K (see Fig. S5 in Sec. E, SI), and find that the PCF for Ga<sub>4</sub>C at this temperature still demonstrates the presence of long-range order, indicating that up to the temperature 650 K, this material remains in a solid state. Thus to ensure the material stability, we adopt the temperature 600 K as the highest temperature to study its thermoelectric conversion efficiency. The predicted ZT at the  $x$ -axis direction versus  $n_h$  and temperature is illustrated in Fig. 4(a). We find that ZT increases with the increasing of tempera-

ture, and the round-peak structure of ZT versus  $n_h$  demonstrates that the maximum value of ZT is 3.28 at 600 K and  $n_h = 5 \times 10^{19} \text{ cm}^{-3}$ . It is inspiring that due to the excellent isotropic characteristics of Ga<sub>4</sub>C, the ultrahigh ZT is ensured in other two axis directions (i.e.,  $y$ - and  $z$ -axis directions, see Fig. S2(e)-(g) in SI). This unique thermoelectric property, i.e., that the high ZT is not influenced by thermal transport directions, proposes another advantage of Ga<sub>4</sub>C as promising thermoelectric material.

To evaluate further the thermoelectric performance of Ga<sub>4</sub>C, we may examine the efficiency of Ga<sub>4</sub>C-based thermoelectric device ( $\eta$ ), which depends mainly on the average ZT, i.e.,  $\overline{ZT}$ , over a wide temperature range described below:

$$\eta = \frac{T_h - T_c}{T_h} \frac{\sqrt{\overline{ZT} + 1} - 1}{\sqrt{\overline{ZT} + 1} + T_c/T_h},$$

where  $\overline{ZT} = \frac{1}{T_h - T_c} \int_{T_c}^{T_h} ZT dT$ . Here  $T_h$  and  $T_c$  represent the temperature in hot and cold sides of thermoelectric devices. We plot the efficiency  $\eta$  over temperature gradients in Fig. 4(b), where

$T_h$  is fixed as 600 K. One can see that in the temperature range of 200-600 K, the maximum efficiency  $\eta_{max}$  as high as 23.5%. It is clear that this efficiency is higher than that of some other thermoelectric materials, such as  $\eta_{max}=19.0\%$  in  $\text{Cs}_3\text{Cu}_2\text{I}_5$ <sup>57</sup>, even the temperature range adopted in latter is much larger than the range considered here. Furthermore, the average  $ZT$  of 2.76 leads to a predicted efficiency of 17.6% over the temperature gradient of 300-600 K with  $n_h = 5 \times 10^{19} \text{ cm}^{-3}$ . Obviously, this efficiency value is also larger than the related values in most thermoelectric materials reported so far under similar conditions. Additionally, the working temperature range adopted here can be easily realized in daily life. Therefore, we believe that  $\text{Ga}_4\text{C}$  is already a high-performance thermoelectric material in ambient conditions.

### 3.5 Large improvements of thermoelectric performance by strain engineering

It has been reported that strain engineering is an effective way to produce band degeneracy and enhance electric conductivity<sup>58,59</sup>. In some materials, lattice strain may bring additional scattering phonons and adjust lattice thermal conductivity<sup>60,61</sup>. Interestingly, our theoretical calculations demonstrate that the tensile strain may reduce remarkably  $\kappa_l$  of  $\text{Ga}_4\text{C}$ . However, the strain engineering does not affect the electronic band degeneracies and the related flat bands, the two key factors responsible for high Seebeck coefficient and large power factor in  $\text{Ga}_4\text{C}$ .

To demonstrate the influences of tensile strain on the thermoelectric performance of  $\text{Ga}_4\text{C}$ , we draw the PF versus  $n_h$  and  $\kappa_l$  versus  $T$  in Figs. 5(a) and 5(b), respectively, where the strain ratio  $\xi$  is set to 0.25%, 0.50% and 0.75%. One may find that as a whole, the PF decreases with increasing  $\xi$ , however reverses at  $\xi=0.75\%$ . To understand this feature, we compare electronic band structures with different tensile strains (see Fig. S6 in Sec. F, SI), and find that these tensile strains rarely affect the band structures or alter new band degeneracy. The PF under constant-relaxation-time approach nearly does not change for different tensile strains (see Fig. S7 in Sec. F, SI). Hence, the strain-induced changing in band structure and  $m_{\text{DOS}}$  can not directly understand the above phenomenon. Then we turn to fall back on the electron relaxation or scattering times changed in strain process. From the previous analyses, we know that POP is the dominant scattering mechanism in  $\text{Ga}_4\text{C}$  and characterized by  $\frac{1}{\tau_{\text{POP}}} \propto N_q \hbar \omega_{\text{PO}} \left( \frac{1}{\epsilon_\infty} - \frac{1}{\epsilon_0} \right)$ , where  $N_q = \frac{1}{e^{\hbar \omega_{\text{PO}}/k_B T} - 1}$  is the number of phonons in each model. At room temperature, the parameter  $\hbar \omega_{\text{PO}}$  in  $\text{Ga}_4\text{C}$  is high to 65.2 meV and  $\frac{1}{\tau_{\text{POP}}}$  increases with the decreasing of  $\omega_{\text{PO}}$ . Additionally, the changing in  $\frac{1}{\epsilon_\infty} - \frac{1}{\epsilon_0}$  is another key factor. Apart from this, we find that the deformation potential scattering can give a small gain to PF, since  $\tau_{\text{ADP}} \propto \frac{C_1}{|m_{\text{DOS}}|^{3/2} \alpha^2}$ , where  $C_1$  is deformation potential coefficient. Note that similar

physical mechanisms from the deformation potential theory has been adopted to explain the enhanced power factors in 3D  $\beta\text{-Cu}_2\text{Se}$ <sup>62</sup> and 2D Te-monolayer<sup>63</sup>. So we conclude that the scattering mechanism is also the key factor for PF variation under strain.

Note that the phonon bands of  $\text{Ga}_4\text{C}$  under different strains are also calculated and provided in Fig. S8 in Sec. F, SI. It is interesting that as the tensile strain increases, the optical branches move downwards and the acoustic branches slightly change. The optical phonons become dominate the lattice thermal conductivity as the strong intermixing of optical and acoustic branches enhance the scattering of acoustic branches (see Fig. S9 in Sec. F, SI), leads to the significant drop of  $\kappa_l$ , as illustrated in Fig. 5(b). It is stressed that as the strain ratio is adopted as 0.75%,  $\kappa_l$  decreases 0.39828  $\text{Wm}^{-1}\text{K}^{-1}$  at 300 K. Overall, the tensile strains reduce further the lattice thermal conductance of  $\text{Ga}_4\text{C}$ . As a result, the maximum  $ZT$  values are enhanced remarkably by the increasing tensile strains as shown in Figs. 5(c)-5(e). Particularly, under the conditions with the strain ratio of 0.75% at 600 K and  $n_h = 5 \times 10^{19} \text{ cm}^{-3}$ ,  $ZT$  may reach over 4.4, which is beyond the  $ZT$  values of most thermoelectric materials reported previously. Therefore, the present studies suggest a real material for the realization of ultrahigh thermoelectric figure of merit and reveal the fundamental mechanisms.

### 3.6 A general roadmap for achieving high thermoelectric performance of $\text{Ga}_4\text{C}$ -family materials

To explore further the high thermoelectric performance in  $\text{Ga}_4\text{C}$ -family materials, in Sec. G, SI, we provided the electronic band structures and the phononic band structures of some other materials including  $\text{X}_4\text{Y}$  ( $\text{X} = \text{B}, \text{Al}$ , and  $\text{Y} = \text{C}, \text{Si}$ ). We find that their electronic and phononic structures are much similar with these of  $\text{Ga}_4\text{C}$ . Especially, the key features in electronic bands for enhancing power factor, such as the electronic band degeneracies, the valley anisotropy and the flat bands, maintain well. Moreover, two crucial factors for decreasing lattice thermal conductance such as the strong phonon scattering and the low phonon group velocity are also generated. These unique properties indicate that the  $\text{Ga}_4\text{C}$ -family materials are a new class of thermoelectric materials with high thermoelectric figure of merit.

Furthermore, one may find that the high thermoelectric performance of  $\text{Ga}_4\text{C}$ -family materials are integrated by multiple effective mechanisms, which are contributed both by the electronic bands and the phononic bands of materials. This property can be regarded as the most attractive characteristic of thermoelectric figure of merit achieved here, since it is much different from almost all thermoelectric materials reported previously. To highlight this finding, we draw a general roadmap for achieving large

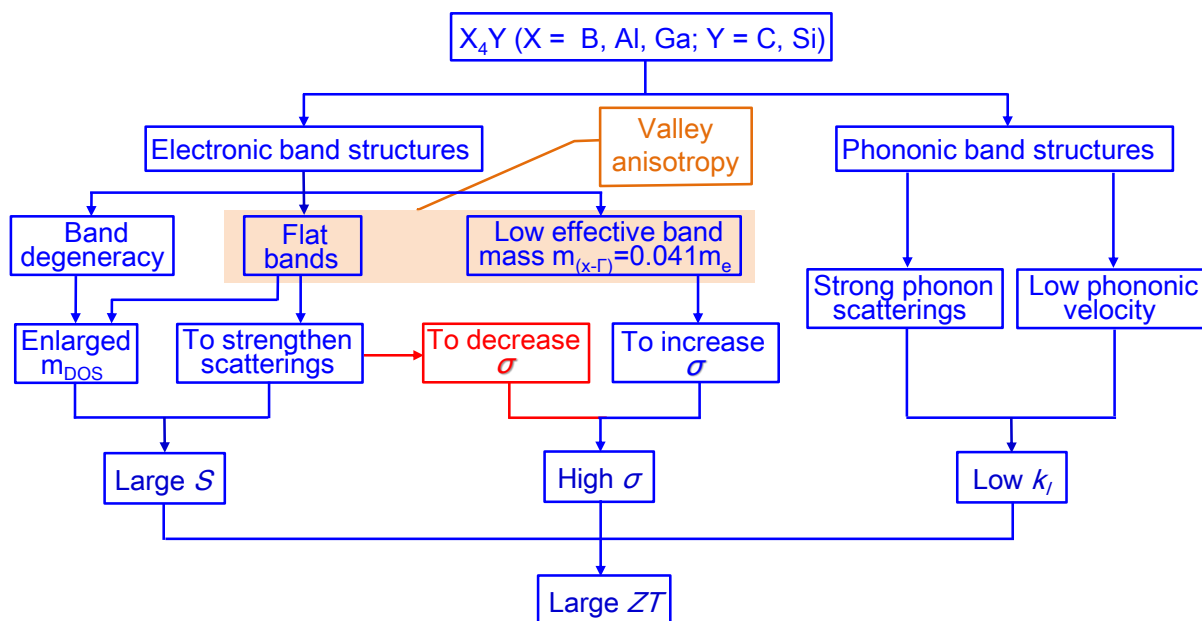


**Fig. 6** A general roadmap for achieving high thermoelectric performance of Ga<sub>4</sub>C-family materials, here the all effective physical mechanisms contributable to the large  $ZT$  are summarized. The contributions from electronic band structure and phononic band structure are listed in the left and right panel, and the valley anisotropy is also highlighted.

$ZT$  in Ga<sub>4</sub>C-family materials in Fig. 6, in which all effective mechanisms obtained here for enhancing  $ZT$  in Ga<sub>4</sub>C are provided. More importantly, this unique characteristic gives the Ga<sub>4</sub>C-family materials several advantages to work as promising thermoelectric materials: (i) we may design many effective ways to improve and regulate their thermoelectric performances. For example, a small tensile strain leads to a ultrahigh  $ZT$  in Ga<sub>4</sub>C. (ii) Based on this family of thermoelectric materials, we can study fully the different roles of various mechanisms on thermoelectric performance in a single material. For example, the flat electronic bands and the low effective band masses constitute two typical features of valley anisotropy in Ga<sub>4</sub>C, nevertheless the former enhances electronic scattering while the latter increases electric conductance, which gives us a chance to study the influence of valley anisotropy on thermoelectric performance. (iii) Ga<sub>4</sub>C-family materials provide us a material plateau to study the competitive effect on thermoelectric performance. For example, as drawn in Fig. 6, the strengthened electrons' scattering may enhance Seebeck parameter and meanwhile decreases electric conductance, however the final PF is still enhanced by electronic scattering. Therefore, these advantages propose that the Ga<sub>4</sub>C-family materials will be developed as a new class of star thermoelectric materials.

## 4 Conclusions

In summary, using the density functional theory combined with Boltzman transport equation, we find a new class of high-performing thermoelectric material, the supertetrahedral Ga<sub>4</sub>C-family materials. Theoretical calculations demonstrate that the high thermoelectric figure of merit of Ga<sub>4</sub>C stems both from large electronic power factor and ultralow lattice thermal conductivity. Particularly, the  $p$ -type Ga<sub>4</sub>C possesses multiple electronic valley degeneracies with  $N_V = 6$  (12) at the high-symmetry point X (W), leading to multi-band degeneracy and further contributing to large electric conductivity. Meanwhile, flat electronic bands connecting two neighboring valleys produce strong inter-valley polar-optical-phonon scattering and hence increase the effective mass and the Seebeck coefficient remarkably. As a result, Ga<sub>4</sub>C has a large power factor up to  $6 \text{ m Wm}^{-1}\text{K}^{-2}$  at 300 K. On the other hand, due to the short phonon lifetimes and small phonon group velocity of Ga<sub>4</sub>C, a ultralow lattice conductivity down to  $0.87 \text{ Wm}^{-1}\text{K}^{-1}$  at 300 K appears in Ga<sub>4</sub>C. Benefiting from high power factor and ultralow lattice thermal conductivity, the  $ZT$  value of Ga<sub>4</sub>C reaches up to 3.28 at 600 K and  $n_h = 5 \times 10^{19} \text{ cm}^{-3}$ .

Furthermore, our investigations uncover that the tensile strain may drastically suppress the lattice thermal conductivity, but retain well other advantages of Ga<sub>4</sub>C such as the multi-valley degeneracies and flat electronic bands. Particularly,  $\kappa_l$  falls to as

low as  $0.398 \text{ Wm}^{-1}\text{K}^{-1}$  under a much small tensile strain ratio 0.75%. Surprisingly, the power factor of  $\text{Ga}_4\text{C}$  is also influenced by tensile strain via boosting the polarized optical phonon scattering and acoustic deformation-potential scattering. Therefore,  $ZT$  value of the strained  $\text{Ga}_4\text{C}$  may become larger than 4.4, a truly colossal thermoelectric figure of merit. By proposing several physical mechanisms to further enhance thermoelectric conversion efficiency, this work opens a new way for the design of high-performing thermoelectric materials, and proposes the  $\text{Ga}_4\text{C}$ -family materials as a new generation of star thermoelectric materials.

## Authors contributions

H. Fu and R. Wu conceived, designed and supervised the study. A. Lu and H. Fu performed the first-principle calculations and Boltzmann transport calculations. A. Lu and H. Fu performed the original draft preparation, and R. Wu and H. Fu finalized the paper. All authors participated in the discussion and analysis of numerical results.

## Conflicts of interest

There are no conflicts to declare.

## Acknowledgements

This work is supported by the National Science Foundation of China with Grants Nos: 11774104, 12147113 and U20A2077. Work at UCI was supported by the US DOE-BES under Grant DE-FG02-05ER46237 and computational time at the National Energy Research Scientific Computing Center.

## Notes and references

- G. J. Snyder and E. S. Toberer, *Nat. Mater.*, 2008, **7**, 105.
- W. Shi, Z. M. Wong, T. Deng, G. Wu and S.-W. Yang, *Adv. Funct. Mater.*, 2021, **31**, 2007438.
- R. A. Kishore, A. Nozariasbmarz, B. Poudel, M. Sanghadasa and S. Priya, *Nat. Commun.*, 2019, **10**, 1765.
- B. Poudel, Q. Hao, Y. Ma, Y. Lan, A. Minnich, B. Yu, X. Yan, D. Wang, A. Muto, D. Vashaee, X. Chen, J. Liu, M. S. Dresselhaus, G. Chen and Z. Ren, *Science*, 2008, **320**, 634–638.
- H. J. Goldsmid *et al.*, *Introduction to thermoelectricity*, Springer, 2010, vol. 121.
- N. Jaziri, A. Boughamoura, J. M. Aijller, B. Mezghani, F. Tounsi and M. Ismail, *Energy Reports*, 2020, **6**, 264–287.
- F. J. DiSalvo, *Science*, 1999, **285**, 703–706.
- L. E. Bell, *Science*, 2008, **321**, 1457–1461.
- B. Anasori, M. R. Lukatskaya and Y. Gogotsi, *Nat. Rev. Mater.*, 2017, **2**, 1–17.
- Y. Wang, L. Yang, X.-L. Shi, X. Shi, L. Chen, M. S. Dargusch, J. Zou and Z.-G. Chen, *Adv. Mater.*, 2019, **31**, 1807916.
- G. Tan, L.-D. Zhao and M. G. Kanatzidis, *Chem. Rev.*, 2016, **116**, 12123–12149.
- L.-D. Zhao, V. P. Dravid and M. G. Kanatzidis, *Energy Environ. Sci.*, 2013, **7**, 251–268.
- W. Ibarra-Hernandez, A. C. Garcia-Castro, A. Bautista-Hernandez, M. Salazar-Villanueva, A. Cantarero and A. H. Romero, *Phys. Rev. Mater.*, 2022, **6**, 025403.
- Y.-J. Zeng, D. Wu, X.-H. Cao, W.-X. Zhou, L.-M. Tang and K.-Q. Chen, *Adv. Funct. Mater.*, 2020, **30**, 1903873.
- L. D. Zhao, H. J. Wu, S. Q. Hao, C. I. Wu, X. Y. Zhou, K. Biswas, J. Q. He, T. P. Hogan, C. Uher, C. Wolverton, V. P. Dravid and M. G. Kanatzidis, *Energy Environ. Sci.*, 2013, **6**, 3346–3355.
- C. Kumarasinghe and N. Neophytou, *Phys. Rev. B*, 2019, **99**, 195202.
- G. Xie, Z. Li, T. Luo, H. Bai, J. Sun, Y. Xiao, L.-D. Zhao, J. Wu, G. Tan and X. Tang, *Nano Energy*, 2020, **69**, 104395.
- Z. Li, C. Xiao, H. Zhu and Y. Xie, *J. Am. Chem. Soc.*, 2016, **138**, 14810–14819.
- T.-H. An, Y. S. Lim, H.-S. Choi, W.-S. Seo, C.-H. Park, G.-R. Kim, C. Park, C. H. Lee and J. H. Shim, *J. Mater. Chem. A*, 2014, **2**, 19759–19764.
- K. Biswas, J. He, I. D. Blum, C.-I. Wu, T. P. Hogan, D. N. Seidman, V. P. Dravid and M. G. Kanatzidis, *Nature*, 2012, **489**, 414–418.
- S. Bhattacharya, A. Bohra, R. Basu, R. Bhatt, S. Ahmad, K. N. Meshram, A. K. Debnath, A. Singh, S. K. Sarkar, M. Navneethan, Y. Hayakawa, D. K. Aswal and S. K. Gupta, *J. Mater. Chem. A*, 2014, **2**, 17122–17129.
- Y. Pei, G. Tan, D. Feng, L. Zheng, Q. Tan, X. Xie, S. Gong, Y. Chen, J.-F. Li, J. He, M. G. Kanatzidis and L.-D. Zhao, *Adv. Energy Mater.*, 2017, **7**, 1601450.
- W. Lin, S.-D. Liang, C. He, W. Xie, H. He, Q. Mai, J. Li and D.-X. Yao, *Sci. Rep.*, 2019, **9**, 1025.
- Y. Dong, C. Zhang, M. Meng, M. M. Groves and J. Lin, *Carbon*, 2018, **138**, 319–324.
- X.-L. Sheng, Q.-B. Yan, F. Ye, Q.-R. Zheng and G. Su, *Phys. Rev. Lett.*, 2011, **106**, 155703.
- J. Zhang, R. Wang, X. Zhu, A. Pan, C. Han, X. Li, Dan Zhao, C. Ma, W. Wang, H. Su and C. Niu, *Nat. Commun.*, 2017, **8**, 683.
- X.-W. Yi, Z. Zhang, Z.-W. Liao, X.-J. Dong, J.-Y. You and G. Su, *Nano Today*, 2022, **42**, 101346.
- I. V. Getmanskii, V. V. Koval, A. I. Boldyrev, R. M. Minyaev and V. I. Minkin, *J. Phys. Chem. A*, 2019, **123**, 267–271.
- I. V. Getmanskii, S. A. Zaitsev, V. V. Koval, R. M. Minyaev and V. I. Minkin, *J. Phys. Chem. A*, 2021, **125**, 6556–6561.

- 30 P. Fu, D.-C. Yang, R. Jia, Z.-J. Yi, Z.-F. Liu, X. Li, R. I. Eglitis and Z.-M. Su, *Phys. Rev. B*, 2021, **103**, 014117.
- 31 I. V. Getmanskii, R. M. Minyaev, D. V. Steglenko, V. V. Koval, S. A. Zaitsev and V. I. Minkin, *Angew. Chem. Int. Ed.*, 2017, **56**, 10118–10122.
- 32 I. V. Getmanskii, V. V. Koval, A. I. Boldyrev, R. M. Minyaev and V. I. Minkin, *J. Comput. Chem.*, 2019, **40**, 1861–1865.
- 33 I. V. Getmanskii, V. V. Koval, R. M. Minyaev, A. I. Boldyrev and V. I. Minkin, *J. Phys. Chem. C*, 2017, **121**, 22187–22190.
- 34 A. Lou, Q.-B. Liu and H.-H. Fu, *Phys. Rev. B*, 2022, **105**, 075431.
- 35 J. He and T. M. Tritt, *Science*, 2017, **357**, eaak9997.
- 36 G. Kresse and J. Furthmüller, 1996, **54**, 11169–11186.
- 37 P. E. Blöchl, *Phys. Rev. B*, 1994, **50**, 17953–17979.
- 38 W. Li, J. Carrete, N. A. Katcho and N. Mingo, *Comput. Phys. Commun.*, 2014, **185**, 1747–1758.
- 39 G. K. H. Madsen, J. Carrete and M. J. Verstraete, *Comput. Phys. Commun.*, 2018, **231**, 140–145.
- 40 A. M. Ganose, J. Park, A. Faghaninia, R. Woods-Robinson, K. A. Persson and A. Jain, *Nat. Commun.*, 2021, **12**, 2222.
- 41 C. Rudderham and J. Maassen, *Phys. Rev. B*, 2021, **103**, 165406.
- 42 S. Wang, Y. Sun, J. Yang, B. Duan, L. Wu, W. Zhang and J. Yang, *Energy Environ. Sci.*, 2016, **9**, 3436–3447.
- 43 Y. Tang, Z. M. Gibbs, L. A. Agapito, G. Li, H.-S. Kim, M. B. Nardelli, S. Curtarolo and G. J. Snyder, *Nat. Mater.*, 2015, **14**, 1223–1228.
- 44 Y. Pei, X. Shi, A. LaLonde, H. Wang, L. Chen and G. J. Snyder, *Nature*, 2011, **473**, 66–69.
- 45 Y. Pei, Z. M. Gibbs, A. Gloskovskii, B. Balke, W. G. Zeier and G. J. Snyder, *Adv. Energy Mater.*, 2014, **4**, 1400486.
- 46 Z.-H. Ge, Y. Qiu, Y.-X. Chen, X. Chong, J. Feng, Z.-K. Liu and J. He, *Adv. Funct. Mater.*, 2019, **29**, 1902893.
- 47 D. I. Bilc, G. Hautier, D. Waroquiers, G.-M. Rignanese and P. Ghosez, *Phys. Rev. Lett.*, 2015, **114**, 136601.
- 48 J. Park, M. Dylla, Y. Xia, M. Wood, G. J. Snyder and A. Jain, *Nat. Commun.*, 2021, **12**, 3425.
- 49 G. J. Snyder, A. H. Snyder, M. Wood, R. Gurunathan, B. H. Snyder and C. Niu, *Adv. Mater.*, 2020, **32**, 2001537.
- 50 S. Lee, K. Esfarjani, T. Luo, J. Zhou, Z. Tian and G. Chen, *Nat. Commun.*, 2014, **5**, 3525.
- 51 Y. Zhao, P. Yu, G. Zhang, M. Sun, D. Chi, K. Hippalgaonkar, J. T. L. Thong and J. Wu, *Adv. Funct. Mater.*, 2020, **30**, 2004896.
- 52 X. Shi, J. Yang, J. R. Salvador, M. Chi, J. Y. Cho, H. Wang, S. Bai, J. Yang, W. Zhang and L. Chen, *J. Am. Chem. Soc.*, 2011, **133**, 7837–7846.
- 53 L. Hu, T. Zhu, X. Liu and X. Zhao, *Adv. Funct. Mater.*, 2014, **24**, 5211–5218.
- 54 Z. Tian, J. Garg, K. Esfarjani, T. Shiga, J. Shiomi and G. Chen, *Phys. Rev. B*, 2012, **85**, 184303.
- 55 J. Tang and J. M. Skelton, *J. Phys.: Condens. Matter*, 2021, **33**, 164002.
- 56 T. Fang, X. Li, C. Hu, Q. Zhang, J. Yang, W. Zhang, X. Zhao, D. J. Singh and T. Zhu, *Adv. Funct. Mater.*, 2019, **29**, 1900677.
- 57 Y.-K. Jung, I. T. Han, Y. C. Kim and A. Walsh, *npj Comput. Mater.*, 2021, **7**, 1–6.
- 58 H. Y. Lv, W. J. Lu, D. F. Shao and Y. P. Sun, *Phys. Rev. B*, 2014, **90**, 085433.
- 59 G. Zhang and Y.-W. Zhang, *Mech. Mater.*, 2015, **91**, 382–398.
- 60 J. Yang, G. P. Meisner and L. Chen, *Appl. Phys. Lett.*, 2004, **85**, 1140–1142.
- 61 S. Li, J. Ma, Y. Pei and Y. Chen, *J. Mater. Chem. C*, 2019, **7**, 5970–5974.
- 62 Y. Xiao, C. Chang, Y. Pei, D. Wu, K. Peng, X. Zhou, S. Gong, J. He, Y. Zhang, Z. Zeng and L.-D. Zhao, *Phys. Rev. B*, 2016, **94**, 125203.
- 63 J. Ma, F. Meng, J. He, Y. Jia and W. Li, *ACS Appl. Mater. Interfaces*, 2020, **12**, 43901–43910.